The Bubbling Galactic Disk II: The Inner 20 Degrees

E. Churchwell, D. F. Watson, M. S. Povich, M. G. Taylor, B. L. Babler, and M. R. Meade

University of Wisconsin–Madison, Dept. of Astronomy, 475 N. Charter Street, Madison, WI 53706

R. A. Benjamin

Department of Physics, University of Wisconsin at Whitewater, 800 West Main Street, Whitewater, WI 53190

R. Indebetouw

Department of Astronomy, University of Virginia, P.O. Box 3818, Charlottesville, VA 22903-0818

and

B. A. Whitney

Space Science Institute, 4750 Walnut St., Suite 205, Boulder, CO 80301

ABSTRACT

We report 269 mid-infrared bubbles within 10° of the Galactic center from visual inspection of the Spitzer GLIMPSE II Legacy Science program images. The main results of this study are as follows. The surface density of bubbles is ∼5 per square degree or about three times that detected in longitudes $|l|$ =10° to 65° because the inner 10° of longitude were more thoroughly searched for small bubbles. There is a gradient in the number of bubbles with longitude with an increase of about a factor of two from 2° to 10°; this is probably the result of several factors including decreasing diffuse background brightness, confusion, and opacity with longitude. Bubble eccentricities are large, typically between 0.6 to 0.8, and >50% show evidence for blow-outs, which we suggest result from local density fluctuations of the ISM and/or anisotropic stellar winds and radiation fields. The average shell thickness of the bubbles scales with the average radius with a slope of ∼0.24; this is shallower than the theoretically predicted asymptotic slope of ∼0.32 because most of the bubbles have not had time to reach the asymptotic value. The fraction of bubbles identified with H II regions and clusters is only about half that found at $|l| > 10°$. This is largely a result of the much

smaller angular diameter of bubbles cataloged in the inner Galaxy than in the outer Galaxy. Finally, at least 12% of the bubbles have morphologies suggestive of triggered star formation. The main difference between the bubbles at $|l| > 10^\circ$ and those at $|l| < 10^\circ$ is that those cataloged in the inner Galaxy are on average smaller than those in the outer Galaxy; this is a selection effect not a physical reality. Most of the bubbles that show evidence for triggered star formation in the inner Galaxy have not formed secondary bubbles; it is postulated that this may be because they are too young to have had time for this to occur. More than 10% of the bubbles have apparent YSOs in projection on their outer boundaries indicative of, but not proof of, triggered star formation.

Subject headings: H II regions — ISM: bubbles — stars: formation

1. Introduction

Infrared dust bubbles surrounding OB clusters and individual O and B stars pervade the disk of the Milky Way and, presumably, other spiral galaxies with active star formation. Infrared dust bubbles first came to the attention of the astronomical community with the infrared (IR) images produced by ISO (Infrared Space Observatory; Kessler et al. 1996) and MSX (Midcourse Space Experiment: Price 1995; Egan et al. 1998; and Price et al. 2001). The GLIMPSE survey (Galactic Legacy Infrared Mid-Plane Survey Extraordinaire; Benjamin et al. 2003), with about 10 times the spatial resolution and 100 times the sensitivity of MSX, has shown that the Galactic disk is teeming with dust bubbles (>1.5 per square degree). A very incomplete catalog of over 320 dust bubbles (Churchwell et al. 2006; hereafter Paper I) has been assembled from the GLIMPSE I (hereafter GI) survey ($|l| = 10^\circ$–65°; $|b| \leq 1^\circ$; fully sampled twice at 3.6, 4.5, 5.8, and 8.0 μm with resolutions from $1.5''$ to $1.9''$). It was argued in Paper I that most of the IR bubbles are produced by O and B stars because the spatial distributions in longitude and latitude of the IR bubbles and O and B stars are similar, more than 25% of the bubbles enclose radio H II regions, 13% or more of the bubbles enclose stellar clusters, and about 60% of the IR bubbles have small angular diameters ($\leq 1'$) and appear to be produced by late B stars whose ultraviolet (UV) radiation is below the threshold to ionize detectable H II regions. Thus, IR bubbles trace recent and continuing star formation in the Galaxy. They provide informative examples of the interaction of recently formed stars with their environments. The dependence of bubble size on wavelength observed, morphology, and integrated infrared luminosity provides constraints on the stellar luminosity, stellar wind strengths, ambient interstellar medium (ISM) densities, dust emission properties as a function of environment, relative motion through the ambient

ISM, and the physics of interfaces of hot, ionized gas with cooler, neutral UV illuminated regions (i.e. Photo-Dissociation Regions; PDRs).

Mid-infrared (MIR) bubbles may be produced by possibly three types of central stars: stars with strong winds, luminous O stars of all luminosity classes and B supergiants; ∼O9 to B3 dwarfs whose winds are too weak to make a significant impact on the structure of the surrounding photo-ionized H II region; and ∼B4 and cooler dwarfs that cannot produce a detectable H II region but have a strong enough radiation field to blow a small dust bubble via radiation pressure. The latter category appears to account for the largest number of MIR dust bubbles, those that are small, have low MIR luminosity, and do not surround a detectable H II region (Churchwell et al. 2006; 2007). Bubbles produced by ∼O9 to B3 dwarfs, in principle, enclose detectable radio H II regions. In the absence significant stellar winds, these H II region will consist of $\sim 10^4$ K photo-ionized gas distributed throughout the volume of the bubble. This is the classical picture of an H II region.

MIR bubbles that surround H II regions produced by stars with strong winds have an entirely different interior structure. The velocity, density, and temperature structure of a stellar wind-blown bubble is quite complicated, both in spatial structure and as a function of age. All three parameters are expected to change by orders of magnitude (at a given age) over small distances at several theoretically predicted boundaries within wind-blown bubbles. Analytic evolution models by Castor, McCray, and Weaver (1975; Weaver et al. 1977; Whitworth et al. 1994; and Capriotti & Kozminsky 2001) predict that wind-blown bubbles around hot OB stars should have the following distinct regions that persist over most of the stellar lifetime: a hypersonic stellar-wind-evacuated cavity immediately around the central star where densities are very low; a hot, low-density, shocked stellar wind region beyond the central cavity that occupies most of the volume of the bubble; a narrow conduction zone where temperature rapidly decreases and density rapidly increases (with radius); and a thin, dense, shell of shocked H^+ gas surrounded by a shell of nonshocked ionized gas. The Weaver et al. (1977) analytic models permit arbitrary ambient densities, but for the most part the analytic models do not anticipate the effects of a bubble expanding into a cold, dense, cloud of molecular gas and dust. For example, Weaver et al. (1977) illustrate their theory by modeling a 10^6 year old bubble expanding into a density of only 1 cm^{-3}. Numerical models by Mellema et al. (2006) have investigated the evolution of H II regions in turbulent molecular clouds and Mizuta et al. (2006) have modeled the formation of pillars at the inner boundaries of expanding H II regions and molecular clouds. Whitworth et al. (1994) examined the properties of shocked gas layers when the layers begin to fragment and trigger star formation.

Recent numerical models of wind blown bubbles around stars of mass 35, 60, and 80

$M_\odot$ by Freyer et al. (2003; 2006), Kröger et al. (2006); and Kröger et al. (2007) confirm the general picture of wind-blown bubbles predicted by the analytic models noted above, but show that the detailed structure can be considerably more complicated due to turbulent interactions and instabilities that can develop at the boundary interfaces. For example, turbulent entrainment causes the sharp boundaries between the hot (10^6 K) and cool (10^4 K) gas to become thicker and to have knots of 10^4 gas entrained in the 10^6 K shell, and the outer shell boundaries can become quite jagged.

Watson et al. (2007) used GLIMPSE, MIPSGAL (24, 70, and 160 μm Spitzer/MIPS images of the GLIMPSE survey area; Carey et al. 2005), and MAGPIS images (20 cm VLA plus Effelsberg single dish data; Helfand et al. 2006), to show that: 24 μm and 20 cm continuum emission (which describes the extent of the H II region) are coincident; the IRAC 8 μm band becomes very bright just outside the H II region ionization-front (I-front) which defines the dust bubble inner radius; and 8 μm brightness slowly declines beyond the bright shell but is clearly present throughout the PDR region of the bubble. The same morphological properties were also observed by Povich et al. (2007) in M17. Based on these observed systematic morphological properties, Paper I, Povich et al. (2007), and Watson et al. (2007) concluded that: 1) dust exists inside H II regions as shown by 24 μm emission lying well inside the H II I-front; 2) features generally attributed to PAHs are destroyed inside bubbles ionized by O and early B stars; and 3) the bright 8 μm shells that define the dust bubbles in the infrared are dominated by PAH emission features excited by soft UV radiation just outside the H II region I-front.

The main goal of this contribution is to extend the bubble catalog of Paper I, which covered only the GI survey area ($10^\circ \leq |l| \leq 65^\circ$ and $b \leq |1|^\circ$), to the GLIMPSE II (hereafter GII) survey area ($b \leq |1|^\circ$ for $|l| = 10^\circ$ to 5°, $|b| \leq 1.5^\circ$ for $|l| = 5^\circ$ to 2°, and $|b| \leq 2^\circ$ for $|l| = 0^\circ$ to 2°). The total GII survey area is 54 square degrees as opposed to 220 square degrees in GI. In the following, we show the spatial distribution and frequency distributions of bubble morphological properties and compare them with those in the GI area. Possible associations with H II regions, planetary nebulae, Wolf-Rayet stars, and supernova remnants are investigated. Evidence for triggered star formation toward $\sim$20% of the bubbles is discussed.

2. The Data

In addition to the GI and GII data, Dr. Susan Stolovy has given us permission to include her Spitzer/IRAC survey of an area of $0.75^\circ \times 0.75^\circ$ centered on the Galactic center (PID 3677 GO program). The properties of the image mosaics from which bubbles were

identified have been described in Paper I. $3^\circ \times 2^\circ$ false color (3.6 μm blue, 5.8 μm green, and 8.0 μm red) image mosaics were systematically and independently searched visually by two of the authors, then a third author checked the two independently selected lists. We provide an on-line, false-color, image archive[1] containing an example of every bubble included in Table 1 (i.e. the extension to the original catalog). The color codes are as stated above. We recommend referring to this archive for bubbles of specific interest. As with the catalog for the GI region, we make no claims for completeness for the GII region. Emphasis has been placed on reliability rather than completeness.

The "elliptical annulus" feature in ds9[2] was used to estimate the approximate center position and the semimajor and semiminor axes of the inner and outer ellipses. The selection effects and measurement biases discussed in Paper I also apply to the bubbles listed in Table 1. The main difference is that two authors first independently identified potential bubbles, then those two critically examined their selections together, discarding bubbles that were not mutually agreed upon. Finally, a third author examined the combined list and only those bubbles that all three agreed upon were included in the final list of bubbles.

The catalog entries in Tables 1 & 2 are arranged in order of increasing angular distance from the Galactic center. The columns in Table 1 are as follows: (1) catalog number preceded by CN if longitude is between 10° and 0° and CS if longitude is between 360° and 350°. The C in the prefix indicates the central region of the Galaxy. Columns (2) & (3) give the center position in Galactic longitude and latitude, respectively; (4) & (5) the semimajor ($R_{\rm in}$) and semiminor ($r_{\rm in}$) axes of the inner ellipse, respectively; (6) & (7) the semimajor ($R_{\rm out}$) and semiminor ($r_{\rm out}$) axes of the outer ellipse, respectively; (8) the eccentricities of the ellipses (the centers and eccentricities of the inner and outer ellipses are constrained to be the same); (9) the average radius $\langle R \rangle$ of the bubble; (10) the average thickness $\langle T \rangle$ of the shell; and, (11) abbreviated morphological flags. We estimate the average radius and shell thickness using equations (1) and (2) in Paper I, respectively. Also, examples of the various morphological types defined by the morphological flags in column 11 of Table 1 are shown in Figure 2 of Paper I.

The morphological flags given in column 11 of Tables 1 & 2 are the same as those in Tables 1 & 2 of Paper I, with the addition of two new flags. We have added the flag BC to designate bubble complexes where several bubbles are located close together in projection but do not overlap, and hence there is no evidence that any of the bubbles have been triggered by one of the other bubbles. The new flag Y designates bubbles that appear to have one or

[1]http://www.astro.wisc.edu/glimpse/bubbles-2/

[2]http://hea-www.harvard.edu/RD/sd9/ref.

more young stellar objects (YSOs) projected within or on its periphery but are too young to have formed detectable secondary bubbles. The MB (multiple bubbles) flag designates bubbles that have smaller, overlapping, secondary bubbles, as defined in Paper I. Figure 1 shows examples of bubbles with Y, BC, and MB flags. We do not show examples of bubbles with other morphological flags because they are well illustrated in Paper I. The dispersions in determinations of morphological properties among the various examiners are about the same as those found in Paper I.

3. The Spatial Distribution of Bubbles

3.1. The Longitude Distribution and Average Surface Density of Bubbles

The distribution of bubbles with distance from the Galactic center is shown in Figure 2. The solid dots represent the sum of bubbles in the 1st and 4th quadrants with angular distance from the Galactic center. Points beyond $l = 10^\circ$ are from GI data but the selection criteria used for GII have been applied to these data. The dashed line is a linear least squares fit to the solid dots; its slope is 2.3. The open symbols show the number of bubbles with distance from the Galactic center in the northern (1st quadrant) and the southern (4th quadrant) halves of the GII survey area separately. For all practical purposes, the distribution of bubbles in the 1st and 4th quadrants are about the same within 10° of the Galactic center. Figure 2 illustrates two important results: 1) the total number of bubbles (sum of the northern and southern halves of the GII survey) systematically increases with distance from the center, amounting to about a factor of 2 increase from $\Delta l = 2^\circ$ to 10°; and, 2) the number of bubbles at l=10° is almost a factor of 4 higher than found in Paper I at this longitude. The latter is entirely because of the greater completeness of small angular diameter bubbles in GII. This is clearly shown by the extension beyond $l = 10^\circ$ to 13° using GI data but with the selection criteria used for the GII region. When taking small bubbles into account in the area $|l| = 10^\circ$–$13^\circ \sim 150$ bubbles were found compared to ∼30 recorded in Paper I. In fact, when including the small bubbles in GI, the number of bubbles continues to smoothly increase beyond $l = 10^\circ$ (see Figure 2). Another reason why one might expect the total density of bubbles to be greater in GII than GI is that the lines of sight through the Galaxy are longer than those through the GI region; however, this is likely to be a negligible effect, as shown in Paper I, because distant bubbles are veiled by foreground emission and the increasing gradient in background brightness toward the Galactic center makes detection more difficult.

We have tabulated 269 bubbles within 10° of the Galactic center in an area of 54 square degrees. This implies an average surface density of about 5 bubbles/square degree, a factor

of slightly more than three greater than the average surface density reported in the GI area; this disparity is entirely due to the incompleteness of small bubbles in GI as shown in Figure 2.

How can we understand the systematic increase in bubbles with angular distance from the Galactic center in GII? This is probably due to a combination of factors that change with increasing distance from the Galactic center, such as decreasing diffuse background brightness, confusion, and opacity. If the circle interior to the central bar is deficient in stars, except in the bar itself, then it is possible that there could be a real gradient in massive stars with distance from the Galactic center. In this case, the trend should continue out to $l \sim 30°$ (Benjamin et al. 2005). Referring to Figure 4 of Paper I, there is a weak tendency for the the total number of bubbles to increase out to $l \sim 30°$, but the dispersion is too large and the number per bin too small to be convincing. Part of the dispersion reflects the fact that stars are not smoothly distributed in the Galactic plane; there are regions where the surface density is high and others where there are very few stars. The trend within 13° of the Galactic center appears to be statistically significant.

3.2. The Latitude Distribution of Bubbles

The distribution of bubbles with Galactic latitude are plotted in Figure 3. All bubbles within a given latitude bin have been summed over all longitudes within 10° of the Galactic center. Note that within $|l| < 5°$ the latitude coverage is greater than for GI (see §1). A double Gaussian with a narrow component and a broad component produces a good fit to the observed distribution as shown in Figure 3. The narrow component has a scale height of $0.23° \pm 0.04°$ and peaks at a latitude of $-0.06° \pm 0.02°$ and the broad component has a scale height of $0.82° \pm 0.013°$. The narrow component suggests a population with scale heights in the range of 20 to 32 pc for distances between 5 to 8 kpc, possibly indicative of the distribution of O and the earliest B stars. This is similar to the scale height found by Becker et al. (1990) for small radio sources at longitudes <50° from the Galactic center, which they argued are probably compact H II regions ionized by extreme Pop I stars. The broad component suggests a population with scale heights in latitude ranging from about 72 to 114 pc for distances between 5 to 8 kpc. This broad component appears to be too small for the Galactic halo population, long-period variables, and RR Lyrae stars, but it does seem to be consistent with old Population I stars or more likely spiral structure supergiants and Cepheids whose scale heights range from ∼100 to ∼60 pc, respectively (Gilmore & Zeilik 1999).

An explanation for why the bubble distribution in both GI and GII peaks at slightly

negative latitudes is probably because the Galactic coordinate system does not correspond to the actual Galactic plane. Support for this hypothesis is provided by the location of SgrA* whose latitude is -0.05° (Reid & Brunthaler 2004). SgrA* is believed to lie at the dynamical center of the Galaxy and, in principle, should lie in the plane of the Galaxy. The discrepancy between the Galactic coordinate system and the actual plane of the Galaxy is a result of forcing the plane as determined by HI radio measurements to pass through the Sun, which at that time was thought to lie in the Galactic plane. In the meantime, we now know that the Sun lies about 10 pc above the plane.

3.3. Bubble Size Distribution

Figure 4 shows the distribution of bubble angular diameters defined as the average of the geometric mean of the inner and outer ellipses (see Eq. 1 in Paper I). Almost 46% of the bubbles in GII have diameters less than $1'$ and 74% have diameters less than $2'$ compared to 17% and 41%, respectively, in GI. The distribution of angular sizes is about the same in GI and GII with the exception that there are more bubbles in the GI catalog than the GII catalog with diameters $>1'$. This is a reflection of the larger GI survey area. The main difference between the distributions of angular sizes between GI and GII is that for diameters $<1'$ the distribution turns down in GI but in GII it sharply increases. This is a result of searching the GII region more thoroughly for small, bright bubbles than was the case for the GI area (see §3.1), and the increased difficulty of detecting faint larger bubbles against the brighter diffuse background in GII than GI.

Figure 5 shows the distribution of bubble diameters with longitude. No statistically significant trend in the angular diameters of bubbles is apparent. Only 6 bubbles have angular diameters greater than $10'$ in the longitude range $|l| < 10°$. The largest angular diameters tend to be found >6° from the center, probably due to lower background levels in these longitude ranges. The vast majority of bubbles are small at all longitudes in GII; only 14 bubbles out of 269 (∼5%) have diameters $>5'$. The mean and median diameters are $\sim 2'$ $\pm$ $0.5'$ and $\sim 1.2' \pm 0.5'$ respectively, at all longitudes, basically unaffected by the few larger bubbles at longitudes >6° from the Galactic center. As noted in Paper I, the main difficulty with detecting large angular diameter bubbles is that they tend to be faint and therefore only detectable in regions of low diffuse background emission. Within 10 degrees of the Galactic center the average infrared background is substantially brighter than in the outer regions of the GI survey area where the largest bubbles were detected. For example, a $10' \times 10'$ box centered at $(l, b) = (5°, 0°)$, in an average region of brightness for the longitude, is more than twice as bright as the same area at $(l, b) = (50°, 0°)$. It is therefore not surprising that

the majority of the bubbles in GII are small (angular diameters typically $<2'$) and bright (especially at 5.8 and 8.0 μm). Although the number of bubbles per unit area in GII is about 3 times that in GI, the fraction of the area covered by bubbles ($\sim$0.9%) is about the same as the GI survey which had an area four times that of GII. This could only be true if the angular size of bubbles reported in GI are larger than those reported in GII.

4. Bubble Morphology

4.1. Shell Thickness

The distribution of bubble thickness to average radius is shown in Figure 6. The distribution peaks between 0.25 and 0.30 with a slower decline for values greater than 0.3 than for those less than 0.3. The distribution in GI peaks at about the same ratio but the width of the distribution is narrower than that in GII. Bubble evolution models predict that the ratio of swept-up ISM shell thickness to its radius should approach asymptotically to a ratio of $\sim$0.32 (see Weaver et al. 1977; Whitworth et al. 1994; Capriotti & Kozminski 2001). So why are some ratios greater than 0.32? One must remember that the models refer to the swept-up gas shell, whereas in the MIR we measure the dust shell emission, which at 5.8 and 8.0 μm is dominated by PAH emission bands and may be more extended than the compressed gas shell. The determination of shell thickness is subjective and not easy to disentangle from the PDR region that extends beyond the swept-up shell, so shell thickness to radius ratios greater than the asymptotic value are not surprising.

The angular shell thickness and average absolute shell thickness are plotted against radius, respectively, in Figure 7 for the GII survey. We do this because the thickness to radius ratio can be modeled as a function of age, stellar luminosity, and density of the ambient ISM. Models predict that $\langle T \rangle / \langle R \rangle$ will reach an asymptotic value of $\sim$0.32 as they age. They reach this asymptote faster with greater ambient ISM density and with lower stellar luminosity (see Weaver et al. 1977; Whitworth et al. 1994). Linear least-squares fits to the observations are shown in Figure 7 as solid lines, and the theoretically predicted asymptotic slope is shown as dashed lines. In Figure 8, the same plots are shown with both GI and GII data combined. Comparison of Figure 8 with Figure 11 in Paper I shows that the average thickness to radius ratio is essentially the same in both GI and GII even though the GII sample contains a much larger percentage of small bubbles. This is interesting because it is harder to obtain accurate thicknesses for the smaller bubbles, and the smaller bubbles are probably younger on average than those in GI. The combination of all bubbles from GI and GII does not change the slope significantly. For the subset of bubbles whose distance is known (right panel of Figs. 7 & 8), the absolute slope is the same as the ratio using angular sizes. We see that

the theoretically predicted asymptotic $\langle T \rangle / \langle R \rangle$ ratio is steeper than the observed value. The fact that the observed slope is flatter than the asymptotic value is probably because in the ensemble of bubbles, many are either too young, too luminous, and/or are expanding into an ambient ISM density that is too low to have reached the asymptotic value. Sorting out which parameter(s) is(are) most important will require further more detailed observations than are presently available.

4.2. Eccentricities

We derive bubble eccentricities using Equation (3) in Paper I. The distribution of bubble eccentricities is shown in Figure 9. The distribution is similar to that for the GI region for eccentricities $\leq$0.5. For eccentricities >0.5, the GI distribution increases more steeply to a peak at $\sim$0.65 and falls off more steeply at eccentricities >0.65 than the GII distribution. Also, the GII distribution peaks at slightly higher eccentricities (0.70−0.75) than that of the GI distribution. These differences are probably not significant given the inherently subjective nature of assigning relatively small differences in morphological properties. Bubble eccentricities and "broken" bubbles (i.e. blow-outs) may result from a non-uniform ambient ISM into which the bubbles are expanding and/or from anisotropic stellar winds and radiation fields (caused, for example, by obstructing circumstellar material such as a disk and/or differences between polar vs equatorial winds). About 53% of the bubbles in GII are broken (i.e. show evidence of blow-out), and 69% have eccentricities >0.5. We find no preference for the orientation of the long axes of the bubbles or the direction of the blow-outs relative to the Galactic plane; the directions are random. We conclude that the large-scale decline of density away from the Galactic plane does not play a significant role in the determination of bubble morphology. If the large eccentricities are primarily the result of confinement by the ambient ISM, we would also conclude that the local density structure is more important than any large scale density gradients away from the Galactic plane. As was noted in Paper I, the large bubble eccentricities and large fraction of broken bubbles seem to imply that the ISM in the Galactic plane is far from uniform and/or that the stellar winds and radiation that drive the bubbles are anisotropic.

5. Association with known objects

Several classes of objects could produce the bubbles in the GII region. Among these are supernova remnants (SNRs), OB stars, Wolf-Rayet (WR) stars, planetary nebulae (PNe), and open clusters. A search of current catalogs of SNRs (Green 2004), PNe (Kerber et al.

2003), WR stars (van der Hucht 2001, 2006), and open clusters (Dutra et al. 2003; Bica et al. 2003) found no positional coincidences with any of the bubbles in GII. However, two bubbles (CS10 and CS14) have mid-IR morphologies very much like those of known PNe, and it is highly probable that they are indeed PNe. Most of the bubbles in GII have small angular diameters, so the fraction of the survey area covered by bubbles is small ($\sim$0.9%). Thus, the probability of a chance alignment of a bubble with another particular class of object is small.

5.1. Overlap with H II Regions

The Paladini et al. (2003) master catalog of H II regions lists 167 H II regions in the GII survey area. 15 H II regions were found that overlap with 14 bubbles in the southern survey area, 13 of which have measured radial velocities from radio recombination lines. Eighteen H II regions were found coincident with 18 bubbles in the northern survey area, 16 of which have measured radial velocities from radio recombination lines. We expect only about one of the 167 H II regions in the Paladini et al. (2003) catalog to align by chance with a bubble in the entire GII survey.

The fraction of bubbles identified with H II regions in GII is only 32/269 $\approx$ 12% or about half the fraction found in GI. We suggest that this is a result of the larger angular diameters of the bubbles in GI than in GII and the suspicion that many of the small, lower luminosity H II regions in GII have probably been missed due to beam dilution, sensitivity limits, and high background brightness in the single-dish radio observations from which most of the sources in the Paladini et al. (2003) catalog have been drawn. At least two-thirds of the bubbles are probably produced by late B stars that do not produce a detectable H II region, which we infer from the fraction of small MIR bubbles that have no corresponding radio continuum counterpart. Of course, single-dish radio surveys may also be incomplete in small diameter HII regions, so the true fraction of small MIR bubbles produced by late B stars is uncertain.

5.2. Association with OB Clusters

Twelve star clusters have been identified in 2MASS data (Dutra et al. 2003) in the northern survey area and 9 in the southern area, but none of these are coincident with GII bubbles. In comparison, 13% of the bubbles in GI are associated with clusters; a sizeable fraction of which were from the Mercer et al. (2005) mid-IR cluster survey. There is no such

survey for the GII region. Clusters are particularly difficult to detect in regions of young massive star formation regions due to bright, diffuse scattered starlight at visible and near infrared wavelengths, and PAH and continuum emission at mid-infrared wavelengths. Extinction is usually high in such regions, especially at visible and near infrared wavelengths. Also, because of the high stellar density within 10 degrees of the Galactic center, stellar clusters are difficult to recognize. Finally, some of the 21 clusters identified by Dutra et al. (2003) may not contain any stars hot enough to produce excess diffuse emission in Spitzer/IRAC bands. Thus identification of compact clusters within the small, MIR-bright bubbles found in GII is expected to be more incomplete than in GI, so it is probably not surprising to find less than 1 in 21 clusters associated with a GII bubble.

6. Bubbles with Known Distances

Of the 32 bubbles that overlap with known H II regions, 29 have measured radial velocities (from the compilation of Paladini et al. 2003) from which kinematic distances can be estimated. The distance ambiguity to one of these, CS55 (H II region G353.41-0.36), was resolved using H I 21 cm absorption line measurements with the VLA (Fish et al. 2003). Near and far distances are given for those whose distance ambiguities have not been resolved. Four bubbles lie near their tangent points and are listed as near distance only. The Galactic rotation model of Brand and Blitz (1993) was used to estimate distances using the IAU standards $R_0 = 8.5$ kpc to the Galactic center and an orbital velocity at R_0 of $\theta = 220$ km s^{-1}. Kinematic distance estimates within 10° of the Galactic center are not very reliable because the assumption of circular motion used to assign distances breaks down. Departures from circular motion along the line of sight are not included in the rotation model and therefore contribute to distance uncertainty. With these caveats, we will proceed on the assumption that the distances derived from radial velocity measurements that are not forbidden by the rotation model are correct and will derive properties based on both the near and far distances when not resolved. Since the probability of chance alignments of H II regions with bubbles is quite small (<1%), the assumption that the bubbles lie at the same distance as the H II regions is a very good one. Table 3 lists the subset of 29 bubbles for which kinematic distances are reported. The column designations are: (1) the bubble designation from Tables 1 or 2; (2) the H II region designation from the Paladini et al. (2003) catalog; (3) the near kinematic distance; (4) the approximate error in distance based on a departure of ∼10 km s^{-1} from circular motions; (5) and (6) the average radius and shell thickness for the near distance in parsecs; (7) the far kinematic distance; (8) the error in kinematic distance assuming ∼10 km s^{-1} departure from circular motion; and (9) and (10) the average radius and shell thickness at the far distance in parsecs. Within 10°

of the Galactic center, the far distance is so much greater than the near distance that only the most luminous bubbles at the far distance are likely to stand out above the foreground diffuse IR emission. So the odds are that most of the bubbles listed in Table 3 are at the near distance. At the near distance, bubble distances range from $\sim$ 0.6 kpc to $\sim$8.5 kpc; there is a slight clustering between 4 to 5 kpc, possibly reflecting citizenship in the molecular ring, but this could also be a result of small number statistics. At the far distance, there is a clustering between 12 to 13 kpc with numbers falling off at both larger and smaller distances.

Bubble radii range from $\sim$0.1 pc to $\sim$4.5 pc, with $\sim$65% having radii less than 2 pc at the near distance. At the far distance, radii range from $\sim$1.4 to $\sim$33 pc and peak between 2$-$4 pc; $\sim$54% have radii $<$5 pc. In the GI survey, bubble radii range from $<$0.1 to 16.9 pc with an average radius of 3.3 pc at the near distance

Bubble shell thicknesses range from $<$0.1 to 1 pc with an average of $\sim$0.4 pc at the near kinematic distance; $\sim$70% have thicknesses of $<$0.5 pc. At the far kinematic distance, the range of thicknesses is 0.6 to 7.6 pc with an average of $\sim$1.9 pc; $>$85% of the bubbles have thicknesses $<$3 pc.

7. Triggered Star Formation

As discussed in §2, we have added two morphological flags in column 11 of Tables 1 & 2 designated by Y and BC. Here we are interested in Y, which flags bubbles whose morphologies suggest candidate protostars on the bubble rims that have not formed detectable secondary bubbles. We also employ the designation MB, which flags bubbles with one or more secondary bubbles located in projection within or on the periphery of the primary bubble. Both Y and MB appear to imply possible triggered star formation by compression of swept-up ISM material by the expansion of the bubble. The difference between Y and MB is that their observed morphologies are different. Bubbles with the Y flag have no secondary bubbles, but they do have MIR sources with morphologies and colors indicative of very young YSOs located within or on the periphery of the projected bubble. The implication seems to be that Y designates young bubbles that have produced YSOs that have not been around long enough to produce their own detectable bubbles. MB, on the other hand, may identify larger and older bubbles that have been around long enough for triggered star formation to have produced secondary bubbles.

A test of the hypothesis that Y bubbles are younger than MB bubbles in principle can be found by comparing their average sizes. In Table 3 we find 10 bubbles with the Y designation in the GII area with known distances, the average radius of which is 2.2 pc at the

near distance. In Table 4 of Paper I, we find 7 bubbles with an MB designation and known distance, the average radius of which is 5.8 pc. Thus, the average radius of Y bubbles in GII are <40% that of the MB bubbles in GI. But since the numbers of Y and MB bubbles with known distances are too small to constitute a meaningful trend, we look to our entire sample of GI and GII bubbles. We have argued that the bubbles are very likely to lie between us and the tangent point. To the extent that angular size is an approximate measure of physical size, and size is an approximate measure of age, it would appear that the average age of Y bubbles is likely to be less than half the age of MB bubbles. The comparison of Y bubbles in GII with MB bubbles in GI, however, could well be misleading because of systematic differences in average ambient ISM densities and possible systematic differences in stellar luminosities. When we compare only the 43 Y bubbles with the 6 MB bubbles in GII with known distances from Table 3, we find average radii of $\sim$1.3$'$ and $\sim$0.9$'$ respectively, which does not support the hypothesis that Y bubbles are smaller and younger than MB bubbles. However, again, one has to be cautious because of small number statistics. It is also possible that the YSOs in some Y bubbles are simply lower luminosity sources than the young stars driving the secondary bubbles in the MB bubbles.

What are YSOs and what criteria do we use to identify them? YSOs are stars in the process of forming. That is, they are still accreting matter through an accretion disk that is being fed from an extended envelope of in-falling matter. Associated with accretion is a bipolar outflow along the spin axis of the protostar, which provides a mechanism to carry off angular momentum. At MIR wavelengths, protostars may have a range of colors that depend on orientation of the accretion disk to the line of sight, the evolutionary state of the protostar, the mass of the in-falling envelope, the temperature and luminosity of the protostar, the mass and geometry of the accretion disk, and possibly other parameters. Observations (Allen et al. 2004) and theory (Robitaille et al. 2006) predict that YSOs have steeply rising spectral energy distributions from 8 μm to 24 μm and hence 8–24 μmcolors should be an effective discriminator of YSOs. In practice, however the diffuse 24 μm dust emission filling the bubbles is often so bright, with such steep gradients toward the bubble rims, that accurate 24 μm photometry or even detection of a YSO candidate on the bubble rim is impossible. Very young protostars generally have steep spectral indices from 3.6–8 μm, and hence can be identified on the basis of their IRAC colors alone. Given these complications, we cannot presently produce a reliably complete catalog of all candidate Y bubbles in GII, but in-depth studies of individual bubbles in the MIR can reliably identify potentially triggered YSOs (Watson et al. 2007). Other observational sign posts of YSOs are association with H_2O and/or CH_3OH masers, location in infrared dark clouds (IRDCs), and coincidence with extended 4.5 μm excess sources (believed to be produced by shocked H_2 or possibly CO outflows from YSOs as inferred from the positional coincidence with a

few independently known YSOs (Smith et al. 2006; Davis et al. 2007).

In the GII region we find 43 bubbles (15.5%) that have Y designations and only 6 (2.2%) MB bubbles; three bubbles have both a Y and MB designations (CN55, CN88, and CN114). Y and MB bubbles together account for nearly 18% of the bubbles in GII that appear to be triggering star formation. This compares with only 6.8% of MB bubbles in the GI survey that show possible evidence of triggering star formation. However, the ratio of ∼7 Y bubbles for each MB bubble in GII suggests, that we probably missed a similar ratio of Y bubbles in GI if this designation had been searched for in GI. We have also probably underestimated the number Y bubbles in GII, as our morphology-based criteria for selecting Y candidates is likely to miss many YSOs that are unresolved. This suggests that a significant fraction of bubbles, at least 18%, show evidence for possible triggered star formation. The implication is that triggered star formation is an important star formation mechanism worthy of further study. We also note that the expansion of bubbles around OB stars into the ambient ISM is not the only mechanism that may trigger star formation. Expanding supernova shells, cloud-cloud collisions, and the impact of star clusters on neighboring molecular clouds have also been suggested as triggering mechanisms.

8. Summary

We have completed the survey for bubbles in the inner Galactic plane by filling in the twenty degrees of longitude ($|l| \leq 10\,^{\circ}$) that were not covered by the GLIMPSE I survey. The surface density of bubbles in GII (∼5 bubbles per square degree) is about three times that in GI (∼1.5 bubbles per square degree), but the fraction of the area covered by bubbles (<1.0%) is about the same in GII and GI. This is because a small fraction of the bubbles in GI are fairly large (radii $>8'$ to $10'$) combined with the fact that the GII area was more thoroughly examined for small bubbles than was the case for GI. The average angular diameter of GII bubbles is only $\sim 2'$ as compared with $\sim 4'$ in GI. The number of bubbles systematically increases by a factor of ∼2 from longitude 2° to 10°. It is suggested that this may be the result of several factors that change with longitude such as decreasing diffuse background brightness, confusion, and opacity with increasing longitude. Morphological properties such as eccentricity and "broken" or discontinuous bubbles (blow-outs) are about the same in GI and GII. Eccentricities are large, most having values between 0.6 and 0.8. More than 50% of the bubbles are discontinuous or show evidence for blow-outs. We suggest that these properties result from local density fluctuations of the ISM and/or anisotropic stellar winds and radiation fields. The average shell thickness scales with radius approximately as $\langle T \rangle \sim 0.24 \langle R \rangle$. This is shallower than the theoretically predicted asymptotic slope of ∼0.32,

possibly because the MIR shells that we measure is may not be the same as the swept-up gas shell predicted by the models.

The fraction of bubbles that overlap with H II regions and known clusters in GII is only about half that found in GI. We suggest that this is a result of the larger angular diameters of the bubbles in GI than in GII and the suspicion that many of the small, lower luminosity H II regions in GII have probably been missed due to beam dilution, sensitivity limits, and high background brightness in the single-dish radio observations from which most of the sources in the Paladini et al. (2003) catalog have been drawn.

At least 18% of the bubbles in GII have morphologies suggestive of triggered star formation. This is a little more than twice the percentage found in GI. However, Paper I did not include many small bubbles and did not look for bubbles with potentially triggered YSOs that have not produced secondary bubbles. Such bubbles are given Y morphological flags in this paper. We suggest that these putative YSOs are either too young or too low-luminosity to produce a detectable secondary bubble. Future work will establish whether the suspected YSOs really are YSOs and that they are at the same distance as the larger bubble with which they coincide in projection. Watson et al. (2007) have carried out a detailed study of three bubbles with known distances from the GI sample and found that two of them have associated YSOs that are good candidates for triggering.

The GI and GII plus Stolovy surveys have highlighted the ubiquity of bubbles in the disk of our Galaxy. The profusion of bubbles seen in the GLIMPSE surveys was only hinted at in earlier IR surveys due to limited sensitivity and spatial resolution. The task for the future will be to use other observational probes to determine the detailed excitation, ionization, and velocity structure of the bubbles to guide determination of better models that can be used to understand how bubbles are driven and interact with the ambient ISM. This will further reveal the consequences of bubble evolution for star formation and injection of kinetic energy into the ISM.

We thank Stephan Jansen who continues to keep our computers online and updated. We acknowledge the IRAC instrument team, who provided the superb camera used to obtain our images. We also acknowledge the continuing support of the staff at the Spitzer Science Center. The MONTAGE software package was used to mosaic the GLIMPSE images. MONTAGE was funded by NASAs Earth Science Technology Office, Computational Technologies Project, under Cooperative Agreement NCC5-626 between NASA and the California Institute of Technology. Dr. Susan Stolovy kindly permitted us to include her data for the area $|l| \leq 1^\circ$, $b \leq 0.75^\circ$ that the GLIMPSE II survey did not include. We are also thank an anonymous referee, who caught several numerical mistakes and made suggestions

that resulted in an improved presentation. Support for this work, part of the Spitzer Space Telescope Legacy Science Program, was funded by NASA through contracts 1275394 and 1282620 to The University of Wisconsin at Madison.

Facilities: Spitzer(IRAC)

REFERENCES

Allen, L. E. et al. 2004, ApJS, 154, 363

Becker, R. H. 1990, ApJ, 358, 485

Benjamin, R. A. et al. 2003, PASP, 115, 953

Benjamin, R. A. et al. 2005, ApJ, 630, L149

Bica, E., Dutra, C. M., Soares, J., & Burbuy, B. 2003, A&A, 404, 223

Brand, J. & Blitz, L. 1993,A&A, 67, 275

Capriotti, E. R. & Kozminsky, J. F, 2001, PASP, 113, 677

Carey, S. J. et al. 2005, BAAS, 207, 63.33

Castor, J., McCray, R. & Weaver, R. 1975, ApJ, 200, L107

Churchwell, E. et al. 2006, ApJS, 649, 759 (Paper I)

Davis, C. J., Kumar, M. S. N., Sandell, G., Froebrich, D., Smith, M. D., & Currie, M. J. 2007, MNRAS, 374, 29

Dutra, C. M. Bica, E., Soares, & J, Barbuy, B. 2003, A&A, 400, 533

Egan, M. P., et al. 1998, ApJ, 494, L199

Fish, V. L., Reid, M. J., Wilner, D. J., & Churchwell, E. 2003, ApJ, 587, 701

Freyer, T., Hensler, G., & Yorke, H. W. 2003, ApJ, 594, 888

Freyer, T., Hensler, G., & Yorke, H. W. 2006, ApJ, 638, 262

Gilmore, G. F., Zeilik, M. 1999, in Allen′s Astrophysical Quantities, 4th Ed., Ed. A. N. Cox, Springer-Verlag, New York, Berlin, Heidelberg, p. 479

Green, D. A. 2004, Bul. Ast. Soc. India, 32, 335

Helfand, D. J., Becker, R. H., White, R. L., Fallon, A., & Tuttle, S. 2006, AJ, 131, 2525

Kerber, F., Mignani, R. P., Guglielmetti, F., Wicenec, A. 2003, A&A, 408, 1029

Kessler, M. F., et al. 1996, A&A, 315, L27

Kröger, D., Hensler, G., Freyer, T. 2006, A&A, 450, L5

Kröger, D., Freyer, T., Hensler, G. Yorke, H. W. 2007, A&A, submitted

Mellema, G., et al. 2006, ApJ, 647, 397

Mercer, E. P. 2005, ApJ, 635, 560

Mizuta, A., et al. 2006, ApJ, 647, 1151

Paladini et al. 2003, A&A, 397, 213

Povich, M. S. et al. 2007, ApJ, 660, 346

Price, S. D. 1995, Space Sci. Rev., 74, 81

Price, S. D., et al. 2001, AJ, 121, 2819

eid, M. J. & Brunthaler, A. 2004, ApJ, 616, 872

Robitaille, T. P. et al. 2006, ApJS, 167, 256

Smith, H. A., Hora, J. L., Marengo, M., & Pipher, J. L. 2006 ApJ, 645, 1264

van der Hucht, K. A. 2001, New Ast. Rev., 45, 135

van der Hucht, K. A. 2006, A&A, 458, 453

Watson, C., et al. 2007, ApJ, submitted

Weaver, R., McCray, R., Castor, J., Shapiro, P., & Moore, R. 1977, ApJ, 218, 377

Whitworth, A. P., et al. 1994, MNRAS, 268, 291

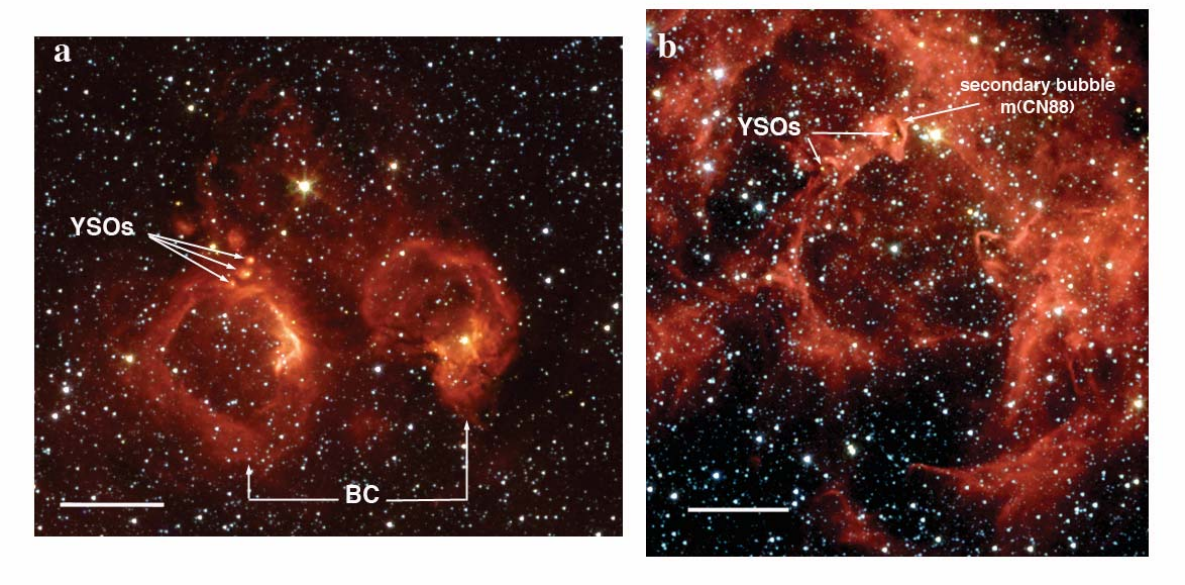

Fig. 1.— Images of bubbles illustrating the three new morphological designations discussed in the text and in col. (11) of Tables 1 and 2. (a) CS44+CS46 present an example of a bubble complex (BC), and CS44 has YSO candidates on its rim (Y). (b) CN88 is a multiple bubble (MB) with a secondary bubble, CN89, on its rim, Y bubble. The horizontal scalebar represents an angular size of 2′.

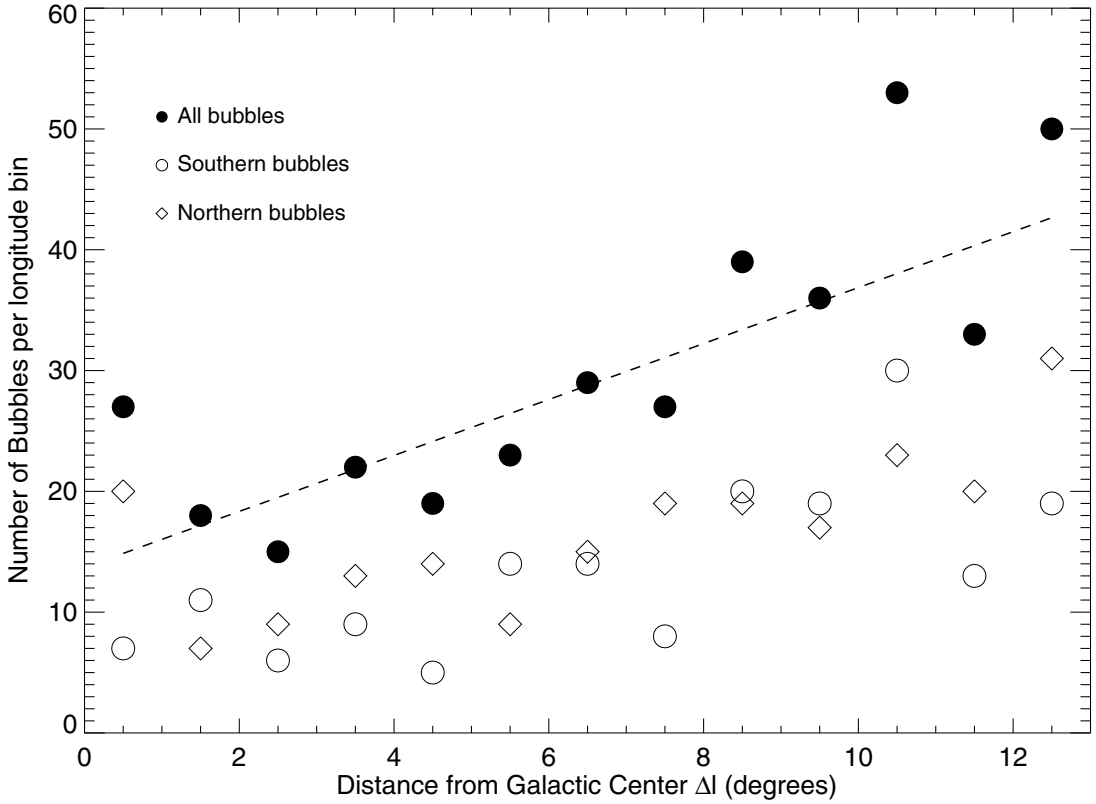

Fig. 2.— The distribution of bubbles with longitude. The sum of bubbles at all longitudes lying within a give angular distance from the Galactic center is shown as solid dots. The dashed line is a linear least squares fit to the solid dots; it has a slope of 2.3. The distribution of bubbles in the north (1st quadrant) and in the south (4th quadrant) are shown separately. The north and south distributions are similar and have about the same slope as the sum (solid dots). This plot has been extended beyond $l = 10^\circ$ to $l = 13^\circ$ using GI data, but applying the same relation criteria used in GII. This shows that both GI and GII data have about the same number of bubbles at $l = 10^\circ$ and the number of bubbles continues to increase at least to $l = 13^\circ$.

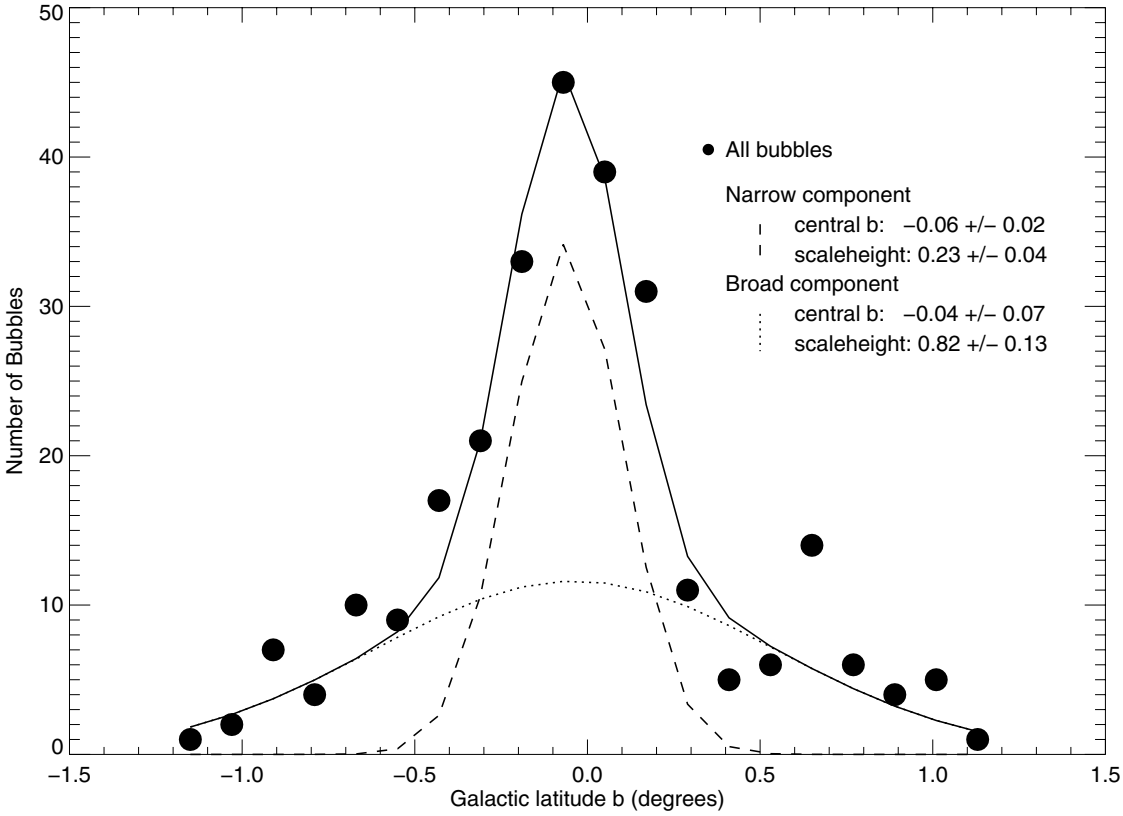

Fig. 3.— The latitude distribution of bubbles lying within 10° of the Galactic center. A two component gaussian was necessary to obtain a satisfactory fit. At each latitude bin, bubbles at all longitudes l<10° have been summed.

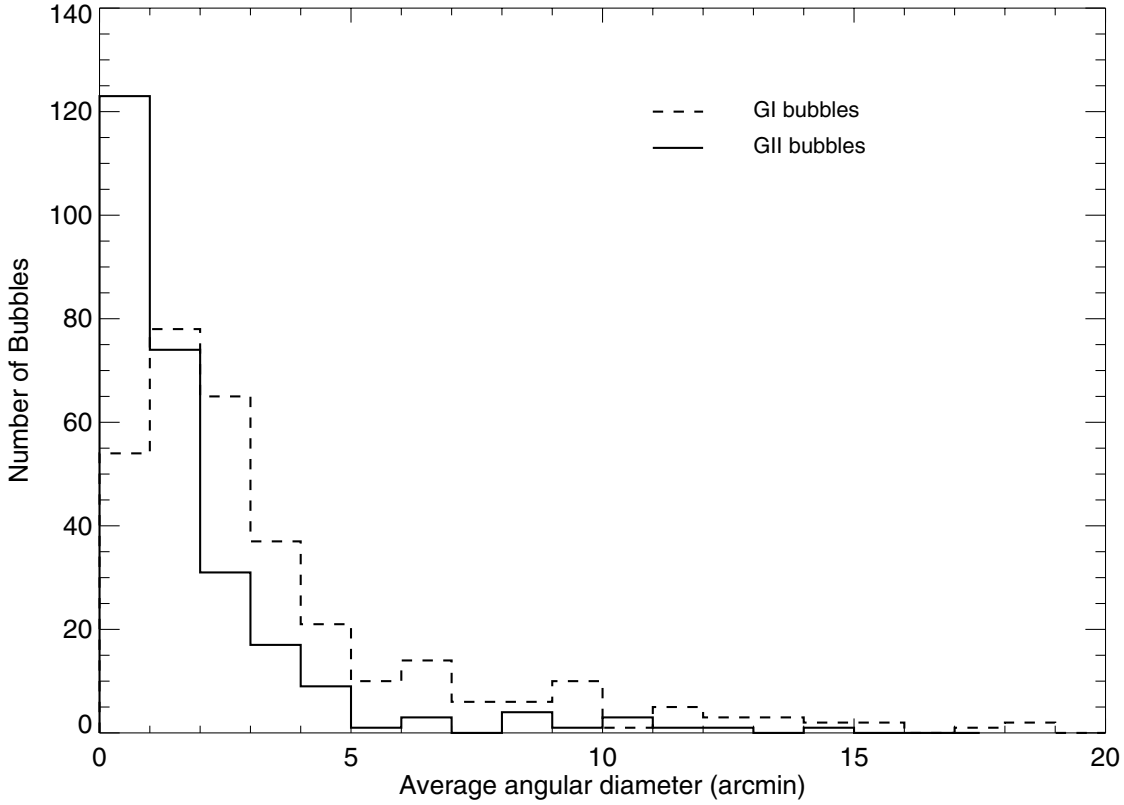

Fig. 4.— The distribution of bubble angular diameters. The dashed curve shows the distribution of bubbles in GI and the solid curve is that of the GII survey.

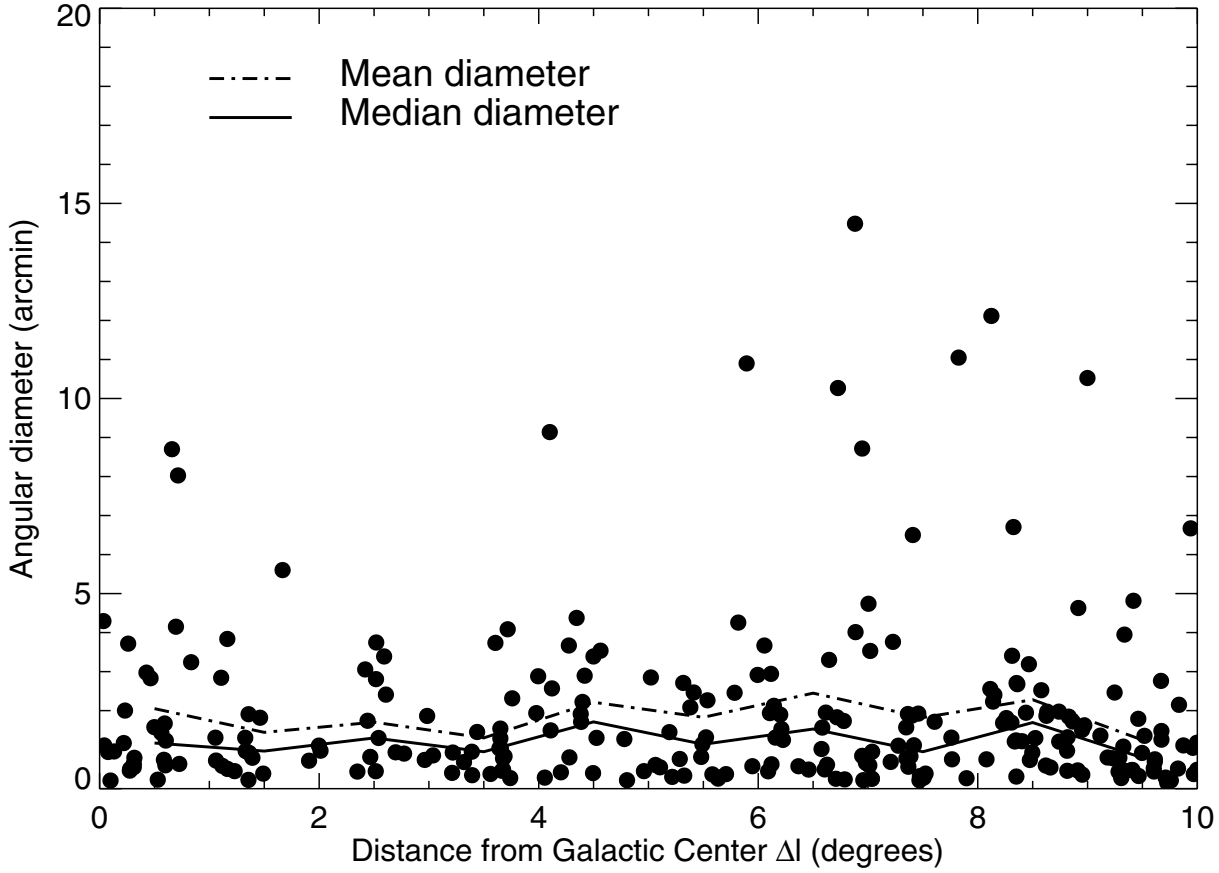

Fig. 5.— The distribution of bubble angular diameters with distance from the Galactic center. Each dot corresponds to a single bubble. The mean and median values are shown for each bin of angular distance from the galactic center.

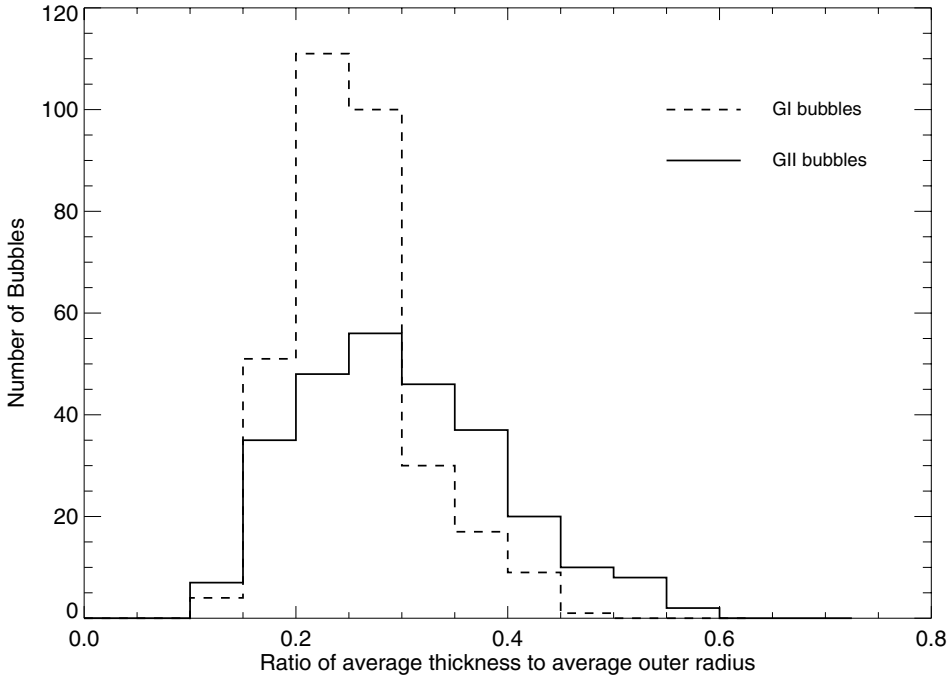

Fig. 6.— The distribution of average bubble thickness-to-radius in both the GI and GII surveys.

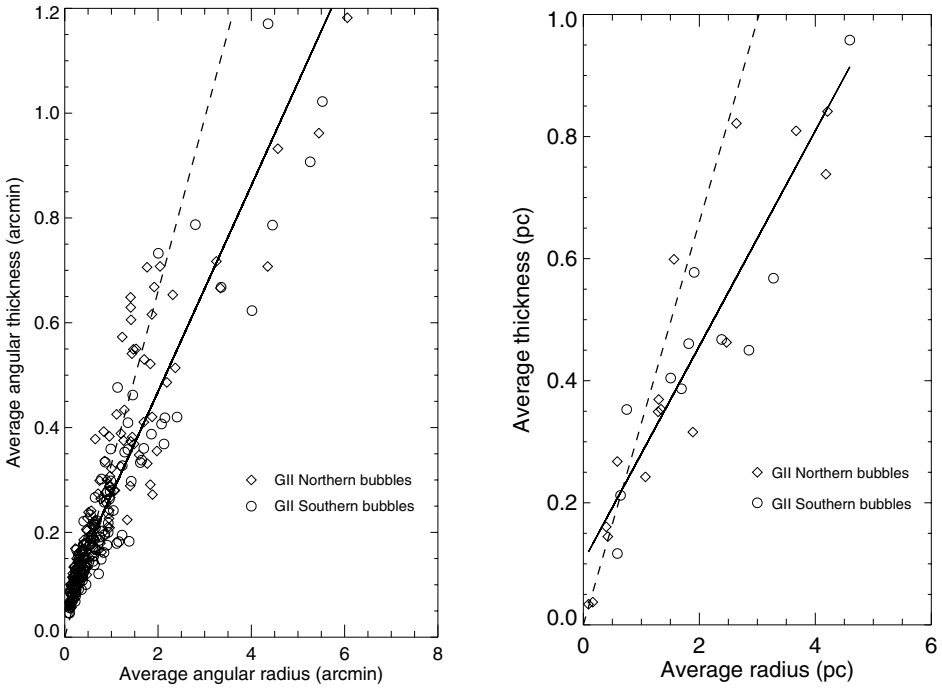

Fig. 7.— The average angular thickness versus average angular radius for bubbles in GII. The solid line is a linear least squares fit to all (northern and southern) data. The dashed line is the theoretically predicted asymptotic ratio. Right panel: The same plot in absolute distance units for the subset of bubbles in GII with known distance. The theoretical asymptote provides, as expected, an upper envelope.

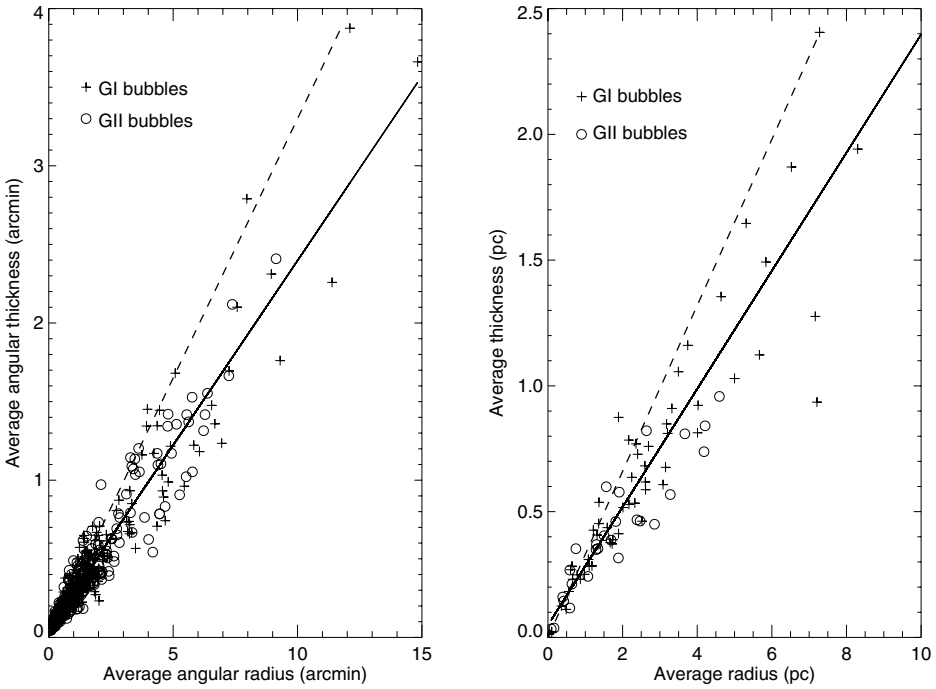

Fig. 8.— Same as Figure 7 except all bubbles from GI and GII are plotted. Note that the observed slopes are basically the same in both plots and practically always less than the theoretical asymptote.

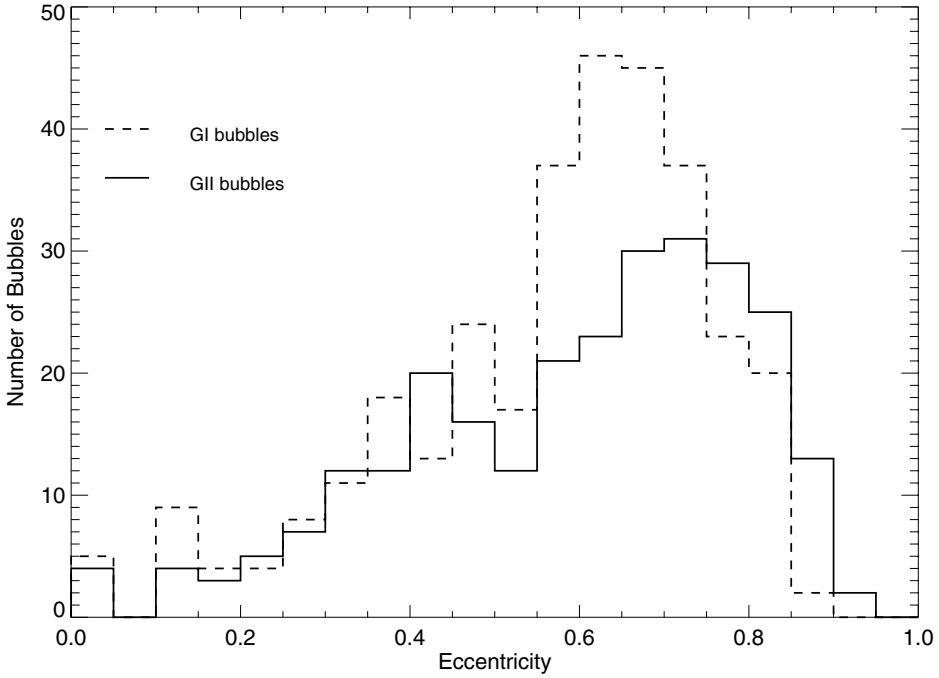

Fig. 9.— The distribution of eccentricities for GI bubbles (dashed curve) and GII bubbles (solid curve).

Table 1. Northern Bubble Parameters

(1) Catalogue number	(2) l (degrees)	(3) b (degrees)	(4) $R_{\rm in}$ (arcmin)	(5) $r_{\rm in}$ (arcmin)	(6) $R_{\rm out}$ (arcmin)	(7) $r_{\rm out}$ (arcmin)	(8) Ecc.	(9) $\langle R \rangle$ (arcmin)	(10) $\langle T \rangle$ (arcmin)	(11) Morphology flags*
CN1	0.042	-0.220	0.54	0.39	0.77	0.55	0.70	0.55	0.19	C,BC
CN2	0.077	-0.206	0.51	0.32	0.67	0.43	0.77	0.47	0.13	B,BC
CN3	0.099	-0.168	0.08	0.07	0.15	0.13	0.48	0.10	0.07	B
CN4	0.132	-0.677	0.47	0.30	0.73	0.46	0.77	0.48	0.20	B,CS
CN5	0.220	0.292	0.58	0.45	0.75	0.58	0.63	0.58	0.16	B
CN6	0.231	-0.504	0.97	0.73	1.34	1.00	0.66	1.00	0.32	C
CN7	0.279	-0.486	0.20	0.16	0.37	0.29	0.62	0.25	0.15	C
CN8	0.311	-0.191	0.24	0.19	0.38	0.30	0.60	0.28	0.13	B,BC
CN9	0.311	-0.205	0.35	0.19	0.51	0.28	0.84	0.32	0.11	B,BC
CN10	0.317	-0.149	0.41	0.27	0.57	0.37	0.76	0.40	0.12	B
CN11	0.427	-0.851	1.47	1.16	1.88	1.48	0.61	1.49	0.37	B,CS
CN12	0.464	-0.657	1.30	0.93	2.04	1.47	0.69	1.41	0.63	B
CN13	0.499	0.155	0.84	0.60	1.03	0.73	0.70	0.79	0.16	B
CN14	0.530	0.183	0.11	0.07	0.17	0.12	0.73	0.12	0.05	C,CS
CN15	0.562	-0.843	0.70	0.48	1.03	0.71	0.73	0.71	0.27	B,BC
CN16	0.586	-0.869	0.34	0.28	0.48	0.39	0.59	0.37	0.13	C,CS,BC
CN17	0.593	-0.846	0.82	0.50	1.32	0.81	0.79	0.84	0.39	C,BC
CN18	0.599	0.331	0.28	0.18	0.46	0.30	0.76	0.30	0.15	B
CN19	0.603	-0.057	0.65	0.42	0.88	0.57	0.76	0.62	0.19	B,Y
CN20	0.659	0.652	4.66	3.43	5.48	4.04	0.68	4.35	0.71	B,CS
CN21	1.055	-0.150	0.72	0.42	1.00	0.58	0.81	0.65	0.22	B
CN22	1.061	-0.234	0.29	0.29	0.43	0.43	0.00	0.36	0.14	C,CS
CN23	1.107	-0.078	1.33	0.94	2.06	1.44	0.71	1.42	0.61	B,BC
CN24	1.163	-0.097	1.98	1.27	2.81	1.81	0.77	1.92	0.67	B,BC,Y
CN25	1.327	0.146	0.62	0.47	0.87	0.67	0.64	0.65	0.22	B,BC
CN26	1.331	0.087	0.42	0.40	0.56	0.54	0.28	0.48	0.14	B,CS,BC
CN27	1.357	0.112	1.18	0.59	1.53	0.76	0.87	0.95	0.24	B,BC
CN28	2.012	-0.682	0.45	0.39	0.59	0.52	0.49	0.49	0.13	B
CN29	2.420	0.080	1.56	1.00	2.25	1.44	0.77	1.53	0.55	B,Y
CN30	2.441	0.481	0.78	0.69	1.07	0.95	0.46	0.87	0.28	B
CN31	2.518	-0.026	1.36	1.17	1.67	1.43	0.51	1.40	0.29	B,Y
CN32	2.520	-0.141	1.80	1.54	2.25	1.93	0.52	1.87	0.42	B,Y

Table 1—Continued

(1) Catalogue number	(2) l (degrees)	(3) b (degrees)	(4) $R_{\rm in}$ (arcmin)	(5) $r_{\rm in}$ (arcmin)	(6) $R_{\rm out}$ (arcmin)	(7) $r_{\rm out}$ (arcmin)	(8) Ecc.	(9) $\langle R \rangle$ (arcmin)	(10) $\langle T \rangle$ (arcmin)	(11) Morphology flags*
CN33	2.608	0.186	1.04	0.98	1.44	1.36	0.33	1.21	0.39	B
CN34	2.697	0.032	0.50	0.30	0.70	0.42	0.80	0.47	0.15	C
CN35	2.773	0.107	0.42	0.31	0.63	0.46	0.68	0.45	0.18	B
CN36	2.962	-0.051	0.29	0.28	0.46	0.44	0.30	0.37	0.16	C,Y
CN37	3.211	-0.104	0.18	0.10	0.36	0.20	0.83	0.20	0.13	C,m(CN38)
CN38	3.217	-0.110	0.47	0.33	0.64	0.44	0.72	0.46	0.14	BMB
CN39	3.320	-0.029	0.36	0.20	0.55	0.31	0.82	0.34	0.14	C,CS
CN40	3.391	0.880	0.42	0.39	0.56	0.52	0.38	0.47	0.14	B,CS,BC
CN41	3.394	0.894	0.12	0.10	0.25	0.22	0.49	0.17	0.12	B,CS,BC
CN42	3.605	-0.215	1.60	1.52	2.23	2.12	0.31	1.87	0.62	B
CN43	3.651	-0.117	0.64	0.64	0.90	0.90	0.11	0.77	0.26	C,BC
CN44	3.665	-0.098	0.20	0.13	0.37	0.23	0.77	0.23	0.13	B,BC
CN45	3.676	-0.101	0.22	0.18	0.32	0.26	0.59	0.24	0.10	C,CS,BC
CN46	3.717	-0.225	1.88	1.51	2.67	2.15	0.59	2.04	0.71	C,CS
CN47	3.741	0.023	0.10	0.09	0.19	0.17	0.48	0.14	0.08	B
CN48	3.978	-0.798	0.90	0.75	1.22	1.02	0.55	0.97	0.29	B,CS,Y
CN49	3.995	-1.011	1.48	0.93	2.16	1.36	0.78	1.44	0.54	B
CN50	4.056	-0.014	0.10	0.09	0.20	0.18	0.32	0.14	0.10	B
CN51	4.101	-1.002	4.30	3.91	5.28	4.80	0.41	4.57	0.93	B
CN52	4.109	0.023	0.69	0.52	1.03	0.78	0.65	0.75	0.30	B
CN53	4.202	-0.026	0.17	0.14	0.28	0.24	0.52	0.21	0.10	C,CS
CN54	4.274	0.035	1.80	1.58	2.11	1.86	0.48	1.83	0.29	B,m(CN54)
CN55	4.280	0.034	0.38	0.28	0.56	0.41	0.68	0.40	0.15	B,MB,Y
CN56	4.345	0.142	2.15	1.76	2.69	2.20	0.57	2.19	0.49	B,Fl,BC
CN57	4.383	0.102	0.82	0.81	1.11	1.09	0.18	0.96	0.29	C,CS,BC
CN58	4.386	0.073	0.81	0.58	1.21	0.87	0.69	0.86	0.34	C,BC
CN59	4.399	0.133	1.25	0.64	1.85	0.95	0.86	1.11	0.43	B,BC
CN60	4.419	0.087	1.29	1.22	1.69	1.59	0.33	1.45	0.38	B,BC
CN61	4.499	-0.959	1.56	1.42	1.99	1.81	0.41	1.69	0.41	B,CS
CN62	4.527	-0.129	0.84	0.37	1.12	0.49	0.90	0.65	0.18	B
CN63	4.563	-0.120	1.80	1.43	2.17	1.73	0.61	1.77	0.33	B,CS
CN64	5.191	-0.282	0.67	0.61	0.84	0.77	0.41	0.72	0.17	B,CS,Y

Table 1—Continued

(1) Catalogue number	(2) l (degrees)	(3) b (degrees)	(4) $R_{\rm in}$ (arcmin)	(5) $r_{\rm in}$ (arcmin)	(6) $R_{\rm out}$ (arcmin)	(7) $r_{\rm out}$ (arcmin)	(8) Ecc.	(9) $\langle R \rangle$ (arcmin)	(10) $\langle T \rangle$ (arcmin)	(11) Morphology flags*
CN65	5.480	-0.238	0.40	0.25	0.63	0.39	0.78	0.41	0.19	C,BC,Y
CN66	5.491	-0.237	0.68	0.30	1.04	0.46	0.90	0.57	0.24	C,BC
CN67	5.524	0.038	0.61	0.49	0.86	0.69	0.59	0.66	0.22	C
CN68	5.629	-0.290	0.12	0.11	0.18	0.17	0.39	0.15	0.06	C,BC
CN69	5.634	-0.291	0.12	0.08	0.19	0.13	0.72	0.13	0.06	C,BC
CN70	5.707	-0.125	0.14	0.12	0.26	0.23	0.42	0.19	0.11	B
CN71	5.894	-0.463	5.17	4.78	6.17	5.70	0.38	5.45	0.96	B,FL,Y
CN72	5.946	-0.141	0.28	0.16	0.47	0.28	0.81	0.29	0.15	B,CS
CN73	6.056	-0.128	1.67	1.48	2.22	1.97	0.46	1.83	0.52	B
CN74	6.107	-0.651	0.83	0.80	1.14	1.10	0.25	0.97	0.31	B,BC
CN75	6.116	-0.149	1.62	0.88	2.36	1.29	0.84	1.47	0.55	B,CS
CN76	6.121	-0.622	0.26	0.22	0.42	0.35	0.56	0.31	0.14	B,BC
CN77	6.143	-0.639	1.08	0.79	1.40	1.03	0.68	1.06	0.28	C,BC,Y
CN78	6.157	-0.609	0.58	0.51	0.81	0.71	0.47	0.65	0.21	C,CC,BC
CN79	6.200	-0.335	0.90	0.77	1.14	0.99	0.51	0.95	0.23	C,CS
CN80	6.211	-0.106	0.71	0.64	0.90	0.81	0.44	0.76	0.18	C
CN81	6.225	-0.028	0.61	0.48	0.79	0.63	0.60	0.62	0.17	C,Y
CN82	6.366	-0.058	0.24	0.18	0.43	0.31	0.69	0.29	0.16	B
CN83	6.576	-0.086	0.40	0.38	0.64	0.62	0.27	0.51	0.24	C
CN84	6.605	-0.082	0.22	0.16	0.35	0.26	0.66	0.25	0.11	C,Y
CN85	6.616	0.143	1.12	0.64	1.47	0.84	0.82	0.98	0.27	B
CN86	6.707	0.187	0.13	0.07	0.21	0.12	0.82	0.13	0.06	B
CN87	6.788	0.226	0.09	0.08	0.16	0.14	0.44	0.12	0.07	B
CN88	7.004	-0.295	2.11	2.11	2.63	2.63	0.00	2.37	0.51	B,MB,Y
CN89	7.011	-0.254	0.24	0.24	0.35	0.35	0.00	0.30	0.11	C,m(CN88)
CN90	7.020	-0.187	1.73	1.15	2.60	1.72	0.75	1.76	0.71	C,MB
CN91	7.034	0.747	0.09	0.06	0.21	0.15	0.70	0.13	0.10	B,BC
CN92	7.035	0.755	0.10	0.07	0.22	0.14	0.76	0.13	0.09	C,BC
CN93	7.038	0.179	0.51	0.34	0.66	0.43	0.75	0.47	0.12	B
CN94	7.207	0.243	0.30	0.28	0.41	0.39	0.36	0.34	0.11	C,CS
CN95	7.227	-0.219	2.51	1.21	2.90	1.40	0.87	1.88	0.27	B
CN96	7.277	-0.062	0.56	0.37	0.79	0.53	0.75	0.55	0.19	C

Table 1—Continued

(1) Catalogue number	(2) l (degrees)	(3) b (degrees)	(4) $R_{\rm in}$ (arcmin)	(5) $r_{\rm in}$ (arcmin)	(6) $R_{\rm out}$ (arcmin)	(7) $r_{\rm out}$ (arcmin)	(8) Ecc.	(9) $\langle R \rangle$ (arcmin)	(10) $\langle T \rangle$ (arcmin)	(11) Morphology flags*
CN97	7.350	0.033	0.31	0.30	0.48	0.47	0.21	0.39	0.16	B
CN98	7.368	-0.115	0.28	0.16	0.47	0.26	0.83	0.28	0.14	C
CN99	7.409	0.684	3.43	2.44	4.28	3.05	0.70	3.25	0.72	B,Y
CN100	7.418	-0.284	0.53	0.39	0.76	0.56	0.68	0.56	0.20	B,CS
CN101	7.458	0.770	1.12	0.66	1.39	0.82	0.81	0.96	0.21	B
CN102	7.469	0.058	0.10	0.06	0.18	0.10	0.82	0.11	0.06	C,BC
CN103	7.473	0.062	0.15	0.11	0.22	0.17	0.63	0.16	0.07	C,BC
CN104	7.507	0.400	0.10	0.08	0.21	0.17	0.60	0.14	0.10	B,CS,BC
CN105	7.524	0.391	0.20	0.10	0.34	0.17	0.87	0.19	0.10	B,CS,BC
CN106	7.760	-0.049	0.57	0.38	1.04	0.69	0.75	0.65	0.38	B
CN107	8.114	0.234	1.29	0.87	1.82	1.22	0.74	1.28	0.43	C,BC
CN108	8.124	-0.465	5.92	5.05	7.20	6.14	0.52	6.06	1.18	C,Y
CN109	8.151	0.242	1.06	1.02	1.39	1.34	0.26	1.20	0.33	C,BC
CN110	8.260	-0.444	0.77	0.74	1.08	1.03	0.30	0.90	0.30	B
CN111	8.312	-0.083	1.52	1.36	2.08	1.86	0.45	1.70	0.53	C
CN112	8.349	0.064	0.59	0.47	0.80	0.64	0.61	0.62	0.19	C
CN113	8.351	-0.319	0.15	0.10	0.24	0.15	0.77	0.15	0.07	C,CS,m(CN114)
CN114	8.361	-0.296	1.26	1.20	1.49	1.41	0.32	1.34	0.22	C,Fl,MB,Y
CN115	8.465	0.119	1.49	1.35	1.86	1.69	0.42	1.60	0.35	C
CN116	8.474	-0.262	0.33	0.29	0.46	0.40	0.50	0.37	0.12	C
CN117	8.497	-0.289	0.37	0.35	0.58	0.55	0.33	0.46	0.21	B
CN118	8.578	-0.686	1.35	0.86	1.82	1.16	0.77	1.26	0.38	C,CS,Y
CN119	8.620	-0.531	0.28	0.22	0.39	0.31	0.62	0.30	0.10	C
CN120	8.662	-0.342	0.22	0.20	0.36	0.32	0.43	0.27	0.13	C,CS
CN121	8.813	-0.019	0.41	0.34	0.66	0.54	0.56	0.49	0.23	C
CN122	8.829	-0.383	0.88	0.76	1.11	0.95	0.52	0.92	0.21	B,Y
CN123	8.865	-0.328	1.15	0.51	1.44	0.64	0.90	0.86	0.20	C
CN124	8.910	0.169	0.19	0.17	0.31	0.27	0.48	0.23	0.11	C,CS
CN125	8.916	-0.499	2.40	1.64	3.19	2.19	0.73	2.32	0.65	B
CN126	9.183	0.045	0.35	0.32	0.48	0.44	0.38	0.40	0.12	B
CN127	9.247	0.185	1.17	0.77	1.87	1.23	0.75	1.23	0.57	C
CN128	9.336	-0.004	1.82	1.77	2.18	2.12	0.22	1.97	0.36	C

Table 1—Continued

(1) Catalogue number	(2) l (degrees)	(3) b (degrees)	(4) $R_{\rm in}$ (arcmin)	(5) $r_{\rm in}$ (arcmin)	(6) $R_{\rm out}$ (arcmin)	(7) $r_{\rm out}$ (arcmin)	(8) Ecc.	(9) $\langle R \rangle$ (arcmin)	(10) $\langle T \rangle$ (arcmin)	(11) Morphology flags*
CN129	9.346	0.183	0.16	0.13	0.35	0.28	0.62	0.23	0.17	C
CN130	9.402	-0.094	0.22	0.15	0.35	0.24	0.71	0.24	0.11	C,BC
CN131	9.408	-0.090	0.22	0.14	0.38	0.24	0.78	0.24	0.13	C,BC
CN132	9.462	0.420	0.99	0.59	1.32	0.79	0.80	0.89	0.26	C
CN133	9.465	-0.850	0.11	0.10	0.23	0.21	0.43	0.16	0.11	B,CS,Y
CN134	9.603	0.199	0.26	0.17	0.38	0.25	0.75	0.26	0.10	C,BC
CN135	9.612	0.196	0.33	0.24	0.48	0.35	0.69	0.34	0.13	C,BC
CN136	9.613	0.206	0.40	0.22	0.61	0.34	0.83	0.38	0.16	C,BC
CN137	9.711	-0.223	0.14	0.08	0.23	0.13	0.82	0.14	0.07	B
CN138	9.833	-0.711	1.00	0.87	1.30	1.14	0.49	1.07	0.28	C,Fl,Y
CN139	9.939	-0.748	3.57	2.53	4.36	3.09	0.71	3.34	0.67	C,Y
CN140	9.959	0.076	0.47	0.43	0.63	0.57	0.42	0.52	0.15	C
CN141	9.968	-0.208	0.15	0.14	0.24	0.22	0.41	0.19	0.09	C
CN142	9.996	-0.032	0.60	0.38	0.87	0.56	0.77	0.59	0.21	C,CS
CN143	10.163	-0.362	0.23	0.16	0.38	0.27	0.70	0.26	0.13	C,CC
CN144	10.164	-0.231	0.41	0.23	0.60	0.33	0.83	0.38	0.14	B,CS
CN145	10.187	-0.398	0.22	0.14	0.37	0.23	0.78	0.23	0.11	C
CN146	10.231	-0.306	0.77	0.76	1.16	1.14	0.18	0.96	0.38	C,Fl
CN147	10.231	0.104	0.26	0.26	0.42	0.42	0.10	0.34	0.16	C,CS
CN148	10.316	-0.131	1.27	0.93	2.03	1.48	0.68	1.41	0.65	C,Y
CN149	10.340	-0.279	1.31	1.15	1.71	1.50	0.48	1.41	0.37	B,Y
CN150	10.460	0.035	0.14	0.10	0.26	0.17	0.75	0.16	0.09	B,BC
CN151	10.472	0.020	0.14	0.11	0.30	0.23	0.63	0.19	0.13	C,BC

*The abbreviations in col.(11) are defined as follows: C is a complete or closed ring. B is a broken or incomplete ring. CC stands for a probable enclosed central star cluster, meaning that the stellar density inside the ring appears to be greater than the average stellar density outside the ring. BC stands for a complex of two or more bubbles, that may or may not be physically associated. Bubbles that have at least one secondary bubble projected within or on its periphery, are labeled MB. Bubbles subsidiary to MB bubbles are labeled m(catalog number) according to the MB bubble they are associated with. Bubbles that have possible YSO(s) projected within or on its periphery but have not formed a secondary bubble, are labelled Y. CS indicates that the central star(s) responsible for driving the bubble is/are probably apparent. Fl indicates a flocculent or clumpy bubble structure. Two bubbles that are probable planetary nebulae are designated by PN.

Table 2. Southern Bubble Parameters

(1) Catalogue number	(2) l (degrees)	(3) b (degrees)	(4) $R_{\rm in}$ (arcmin)	(5) $r_{\rm in}$ (arcmin)	(6) $R_{\rm out}$ (arcmin)	(7) $r_{\rm out}$ (arcmin)	(8) Ecc.	(9) $\langle R \rangle$ (arcmin)	(10) $\langle T \rangle$ (arcmin)	(11) Morphology flags*
CS1	359.965	-0.502	2.25	1.67	2.74	2.03	0.67	2.15	0.42	B,Y
CS2	359.740	-0.411	1.71	1.63	2.10	2.00	0.30	1.86	0.39	B,FL,Y
CS3	359.725	-0.372	0.21	0.17	0.30	0.24	0.58	0.23	0.08	C,CS
CS4	359.305	-0.245	2.11	1.66	2.57	2.02	0.62	2.08	0.41	B
CS5	359.286	0.295	3.83	3.58	4.47	4.18	0.35	4.01	0.62	C
CS6	359.274	-0.042	0.29	0.24	0.41	0.33	0.57	0.32	0.10	C,CS
CS7	359.166	-0.308	1.61	1.31	1.98	1.61	0.58	1.62	0.33	B
CS8	358.883	0.059	0.24	0.19	0.42	0.33	0.60	0.29	0.16	B
CS9	358.835	-0.741	0.21	0.14	0.42	0.27	0.76	0.25	0.17	B
CS10	358.770	0.109	0.20	0.19	0.27	0.25	0.31	0.22	0.07	C,CS,PN
CS11	358.644	-0.481	0.07	0.07	0.16	0.15	0.22	0.11	0.09	C
CS12	358.637	0.068	0.41	0.41	0.51	0.51	0.13	0.46	0.10	C
CS13	358.608	-0.058	0.45	0.21	0.71	0.33	0.89	0.40	0.18	B,Y
CS14	358.538	0.130	0.90	0.75	1.09	0.91	0.55	0.91	0.18	C,CS,PN
CS15	358.510	-0.367	0.15	0.13	0.26	0.23	0.44	0.19	0.10	C,CS
CS16	358.333	-0.748	2.88	2.01	3.83	2.67	0.72	2.80	0.79	B
CS17	358.092	-0.429	0.32	0.30	0.42	0.39	0.36	0.36	0.09	B
CS18	358.002	-0.165	0.50	0.38	0.76	0.59	0.64	0.55	0.23	B
CS19	357.652	-0.062	0.21	0.14	0.32	0.22	0.72	0.22	0.09	B
CS20	357.534	0.198	0.30	0.30	0.52	0.52	0.13	0.41	0.22	C
CS21	357.484	-0.034	0.19	0.13	0.35	0.24	0.73	0.22	0.13	B
CS22	357.459	0.613	0.69	0.38	1.05	0.58	0.83	0.65	0.27	C
CS23	357.408	0.670	2.04	1.12	2.53	1.39	0.84	1.69	0.36	B
CS24	357.016	-0.123	0.90	0.77	1.12	0.95	0.53	0.93	0.20	B
CS25	356.963	-0.044	0.38	0.34	0.52	0.47	0.43	0.43	0.13	B,CS
CS26	356.561	-0.080	0.74	0.60	0.87	0.71	0.58	0.73	0.12	B
CS27	356.439	0.111	0.14	0.13	0.25	0.24	0.28	0.19	0.11	B
CS28	356.358	0.229	0.50	0.40	0.66	0.52	0.60	0.52	0.14	B,CS,BC
CS29	356.349	-0.230	0.72	0.44	0.93	0.57	0.79	0.64	0.17	C,BC
CS30	356.344	0.215	0.44	0.40	0.64	0.58	0.42	0.51	0.19	B,CS,BC
CS31	356.325	-0.235	0.40	0.27	0.54	0.37	0.72	0.39	0.12	B,CS,BC
CS32	356.311	-0.198	0.42	0.30	0.56	0.40	0.70	0.41	0.13	C,BC

Table 2—Continued

(1) Catalogue number	(2) l (degrees)	(3) b (degrees)	(4) $R_{\rm in}$ (arcmin)	(5) $r_{\rm in}$ (arcmin)	(6) $R_{\rm out}$ (arcmin)	(7) $r_{\rm out}$ (arcmin)	(8) Ecc.	(9) $\langle R \rangle$ (arcmin)	(10) $\langle T \rangle$ (arcmin)	(11) Morphology flags*
CS33	356.241	0.667	1.29	0.88	1.51	1.03	0.73	1.16	0.18	B
CS34	355.879	-0.522	1.21	1.01	1.60	1.34	0.55	1.28	0.35	B
CS35	355.505	-0.062	0.15	0.14	0.26	0.24	0.37	0.20	0.11	B
CS36	355.220	-0.014	0.58	0.55	0.72	0.69	0.29	0.64	0.14	C
CS37	355.195	-0.036	0.08	0.08	0.14	0.14	0.00	0.11	0.07	B
CS38	355.041	-0.400	0.26	0.11	0.43	0.18	0.91	0.22	0.11	C
CS39	354.978	-0.532	1.45	1.12	1.79	1.38	0.64	1.43	0.30	C,Y
CS40	354.937	0.331	0.30	0.18	0.48	0.29	0.80	0.30	0.14	C
CS41	354.895	-0.222	0.26	0.19	0.39	0.28	0.70	0.27	0.11	B
CS42	354.784	0.827	0.12	0.10	0.21	0.17	0.59	0.15	0.08	B,CS
CS43	354.715	0.297	0.38	0.28	0.51	0.37	0.70	0.38	0.11	C,Y
CS44	354.683	0.473	1.18	1.12	1.60	1.52	0.31	1.35	0.41	C,BC,Y
CS45	354.674	0.245	0.15	0.11	0.24	0.18	0.68	0.17	0.08	C
CS46	354.619	0.492	0.99	0.86	1.25	1.08	0.50	1.04	0.24	C,BC,Y
CS47	354.588	0.005	1.13	1.01	1.47	1.33	0.43	1.23	0.33	C,CS,Y
CS48	354.462	0.070	0.93	0.86	1.42	1.32	0.36	1.13	0.48	C
CS49	354.418	0.034	0.16	0.12	0.27	0.19	0.70	0.18	0.09	C
CS50	354.216	0.979	1.18	1.08	1.38	1.27	0.39	1.23	0.19	B
CS51	354.182	-0.053	2.07	1.83	2.46	2.17	0.47	2.13	0.37	C,Y
CS52	354.005	0.614	1.72	0.87	2.37	1.20	0.86	1.46	0.46	B
CS53	353.910	0.561	0.17	0.16	0.29	0.28	0.33	0.22	0.12	B,CS
CS54	353.541	-0.457	0.24	0.16	0.35	0.24	0.73	0.24	0.09	B,CS
CS55	353.417	-0.375	1.11	0.45	1.34	0.55	0.91	0.78	0.15	B
CS56	353.374	-0.335	0.25	0.24	0.37	0.36	0.28	0.31	0.11	B
CS57	353.354	-0.138	1.58	1.38	1.95	1.70	0.49	1.65	0.34	C,Y
CS58	353.283	-0.477	0.89	0.67	1.21	0.92	0.66	0.91	0.28	B
CS59	353.274	0.595	5.78	3.43	7.54	4.48	0.80	5.13	1.36	B,BC
CS60	353.220	-0.260	0.83	0.59	1.22	0.88	0.70	0.87	0.33	C
CS61	353.118	0.855	8.38	4.90	10.56	6.17	0.81	7.24	1.66	C,BC
CS62	353.113	0.337	2.29	1.17	3.31	1.70	0.86	2.01	0.73	B,BC
CS63	353.053	0.625	4.90	2.91	6.42	3.81	0.81	4.36	1.17	B,BC
CS64	353.053	-0.014	0.35	0.34	0.51	0.48	0.33	0.42	0.15	B,MB

Table 2—Continued

(1) Catalogue number	(2) l (degrees)	(3) b (degrees)	(4) $R_{\rm in}$ (arcmin)	(5) $r_{\rm in}$ (arcmin)	(6) $R_{\rm out}$ (arcmin)	(7) $r_{\rm out}$ (arcmin)	(8) Ecc.	(9) $\langle R \rangle$ (arcmin)	(10) $\langle T \rangle$ (arcmin)	(11) Morphology flags*
CS65	353.043	-0.018	0.10	0.07	0.17	0.11	0.74	0.11	0.06	C,m(CS64)
CS66	353.019	-0.842	0.28	0.25	0.42	0.38	0.42	0.33	0.14	B
CS67	352.652	-0.364	0.75	0.54	1.11	0.79	0.70	0.79	0.30	C,CS,BC
CS68	352.637	-0.350	1.07	0.64	1.41	0.84	0.80	0.96	0.26	B,BC
CS69	352.613	0.178	0.38	0.28	0.58	0.43	0.68	0.41	0.18	B
CS70	352.601	-0.179	0.93	0.72	1.20	0.93	0.64	0.94	0.24	B,CC,Y
CS71	352.393	-0.065	0.93	0.62	1.17	0.78	0.75	0.86	0.20	C,CS
CS72	352.235	-0.152	0.36	0.28	0.49	0.39	0.60	0.38	0.11	B,CS
CS73	352.174	0.297	5.65	4.45	6.80	5.35	0.62	5.52	1.02	B
CS74	352.103	0.162	0.10	0.08	0.19	0.16	0.55	0.13	0.09	C
CS75	351.921	0.644	0.36	0.24	0.56	0.38	0.74	0.38	0.17	C,CS
CS76	351.861	0.199	1.09	0.97	1.28	1.13	0.46	1.12	0.18	C
CS77	351.769	0.100	0.92	0.63	1.12	0.76	0.73	0.84	0.16	B,Y
CS78	351.694	0.653	0.77	0.67	1.05	0.90	0.51	0.85	0.26	B,CC
CS79	351.675	0.516	3.13	2.91	3.82	3.56	0.36	3.35	0.67	C,Fl
CS80	351.663	0.159	0.54	0.49	0.73	0.66	0.42	0.60	0.17	C,BC
CS81	351.646	0.165	1.55	0.89	2.02	1.16	0.82	1.35	0.36	B,BC
CS82	351.597	0.157	0.57	0.50	0.72	0.64	0.47	0.61	0.14	C,BC
CS83	351.561	0.198	0.84	0.83	1.12	1.10	0.17	0.97	0.28	B,CS
CS84	351.476	-0.460	0.70	0.42	0.98	0.58	0.80	0.65	0.21	C
CS85	351.375	0.642	0.94	0.72	1.19	0.91	0.64	0.93	0.22	C
CS86	351.367	0.690	1.13	0.57	1.64	0.83	0.86	0.99	0.36	C
CS87	351.261	1.018	0.98	0.71	1.34	0.97	0.69	0.99	0.30	C,CS
CS88	351.258	0.679	0.57	0.45	0.78	0.62	0.60	0.60	0.19	C
CS89	351.185	0.698	0.21	0.17	0.30	0.24	0.59	0.23	0.08	B,CS,Y
CS90	351.182	0.483	0.62	0.50	0.85	0.69	0.59	0.66	0.21	C
CS91	351.050	-0.322	0.81	0.53	1.05	0.69	0.75	0.75	0.19	C,CS
CS92	351.048	-0.393	0.16	0.13	0.24	0.19	0.60	0.18	0.07	B,CS
CS93	351.030	0.154	0.86	0.59	1.10	0.76	0.73	0.81	0.20	B,Y
CS94	351.001	0.646	5.64	4.10	6.71	4.87	0.69	5.26	0.91	B
CS95	350.883	0.730	0.67	0.48	0.94	0.67	0.70	0.68	0.22	C
CS96	350.770	-0.077	0.39	0.27	0.55	0.38	0.72	0.39	0.13	C,Y

Table 2—Continued

(1) Catalogue number	(2) l (degrees)	(3) b (degrees)	(4) $R_{\rm in}$ (arcmin)	(5) $r_{\rm in}$ (arcmin)	(6) $R_{\rm out}$ (arcmin)	(7) $r_{\rm out}$ (arcmin)	(8) Ecc.	(9) $\langle R \rangle$ (arcmin)	(10) $\langle T \rangle$ (arcmin)	(11) Morphology flags*
CS97	350.718	1.045	0.18	0.14	0.31	0.25	0.61	0.22	0.12	B
CS98	350.710	0.999	0.38	0.26	0.58	0.40	0.73	0.40	0.17	C
CS99	350.693	-0.492	0.14	0.08	0.22	0.13	0.80	0.14	0.06	B
CS100	350.674	0.836	0.52	0.39	0.72	0.55	0.65	0.54	0.18	B,CS
CS101	350.582	-0.067	2.60	1.86	3.09	2.22	0.70	2.41	0.42	B
CS102	350.504	0.968	0.43	0.31	0.65	0.46	0.70	0.46	0.18	C,CS,BC
CS103	350.481	0.949	0.69	0.51	0.88	0.66	0.66	0.68	0.17	C,BC
CS104	350.395	-0.058	0.19	0.17	0.27	0.25	0.41	0.22	0.08	C
CS105	350.331	0.152	1.51	1.10	1.72	1.26	0.68	1.38	0.18	B,Y
CS106	350.327	0.096	0.79	0.53	1.02	0.68	0.75	0.74	0.18	B,CS
CS107	350.327	-0.008	0.67	0.41	0.94	0.57	0.79	0.63	0.21	B
CS108	350.277	0.113	0.13	0.07	0.21	0.12	0.83	0.13	0.06	B,BC
CS109	350.275	0.119	0.06	0.05	0.11	0.09	0.55	0.08	0.05	C,BC
CS110	350.241	0.062	0.10	0.07	0.15	0.11	0.69	0.10	0.05	C,CS
CS111	350.176	0.016	0.22	0.20	0.32	0.29	0.44	0.26	0.10	B
CS112	350.127	0.070	0.64	0.34	0.89	0.47	0.85	0.55	0.18	B
CS113	350.001	0.429	0.20	0.19	0.29	0.28	0.22	0.24	0.09	B
CS114	349.925	0.083	0.14	0.14	0.23	0.22	0.36	0.18	0.08	B
CS115	349.892	0.243	0.32	0.20	0.44	0.27	0.78	0.30	0.09	C,Y
CS116	349.810	-0.605	4.36	3.78	5.21	4.51	0.50	4.45	0.79	B
CS117	349.777	0.115	0.60	0.49	0.77	0.63	0.57	0.62	0.15	B
CS118	349.477	0.121	0.46	0.23	0.62	0.31	0.87	0.38	0.12	B,CS,Y

*See footnote to Table 1.

Table 3. Sizes and Thicknesses of Bubbles with Known Kinematic Distances

Catalogue #	HII #[a]	Near Kinematic Distance[b]				Far Kinematic Distance			
		D (kpc)	δD (kpc)	$\langle R \rangle$ (pc)	$\langle T \rangle$ (pc)	D (kpc)	δD (kpc)	$\langle R \rangle$ (pc)	$\langle T \rangle$ (pc)
CN15	10	7.5	0.9	1.6	0.6	9.5	0.9	2.0	0.8
CN43	33	1.9	2.1	0.4	0.1	15.1	2.1	3.4	1.2
CN63	43	4.8	1.1	2.5	0.5	12.1	1.1	6.2	1.2
CN64	50	0.8	2.6	0.2	0.0	16.2	2.6	3.4	0.8
CN65	60	5.0	0.8	0.6	0.3	12.0	0.8	1.4	0.6
CN71	65	2.6	2.2	4.2	0.7	14.3	2.2	22.6	4.0
CN73	70	2.4	2.2	1.3	0.4	14.5	2.2	7.7	2.2
CN77	69	4.3	1.0	1.3	0.4	12.6	1.0	3.9	1.0
CN99	100	3.9	1.0	3.7	0.8	13.0	1.0	12.3	2.7
CN103	101	8.4	0.0	0.4	0.2				
CN109	109	3.7	1.0	1.3	0.3	13.1	1.0	4.6	1.2
CN111	112	5.3	0.5	2.6	0.8	11.5	0.5	5.7	1.8
CN114	114	4.8	0.6	1.9	0.3	12.0	0.6	4.7	0.8
CN123	199	4.3	0.7	1.1	0.2	12.5	0.7	3.1	0.7
CN135	121	0.9	3.0	0.1	0.0	15.9	3.0	1.6	0.6
CN139	128	4.3	0.7	4.2	0.8	12.4	0.7	12.0	2.4
CS2	1440	8.5	0.0	4.6	1.0				
CS4	1436	4.0	0.7	2.4	0.5	13.0	0.7	7.9	1.5
CS33	1424	8.5	0.0	2.9	0.5				
CS40	1418	8.5	0.0	0.7	0.4				
CS44	1417	4.9	0.9	1.9	0.6	12.1	0.9	4.8	1.4
CS51	1411	5.3	0.7	3.3	0.6	11.6	0.7	7.2	1.2
CS55[c]	···	3.8	2.4	0.9	0.2				
CS61[d]	1398+1404	1.2	2.7	2.6	0.6	15.7	2.7	33.0	7.6
CS63	1401	1.2	2.7	1.5	0.4	15.7	2.7	19.9	5.3
CS70	1391	6.7	0.2	1.8	0.5	10.2	0.2	2.8	0.7
CS71	1389	6.8	0.2	1.7	0.4	10.1	0.2	2.5	0.6
CS79	1386	0.6	3.0	0.6	0.1	16.2	3.0	15.8	3.2
CS84	1380	3.4	1.1	0.6	0.2	13.4	1.1	2.5	0.8

[a]Catalog number from the Paladini et al. (2003) catalog of Galactic H II regions.

[b]When a bubble lies at the tangent point, no far kinematic distance is given, and the near kinematic distance is the tangent point distance.

[c]Distance determined from 21 cm absorption Fish et al. (2003).

[d]Distance determined from two H II regions found within the bubble.